




Relationship between molecular structure and corrugations in self-assembled polypeptoid nanosheets revealed by cryogenic electron microscopy

Xi Jiang ^{1,*}, Ronald N. Zuckermann ², and Nitash P. Balsara ^{1,3,†}

¹Materials Sciences Division, Lawrence Berkeley National Laboratory, Berkeley California 94720, USA

²Molecular Foundry, Lawrence Berkeley National Laboratory, Berkeley California 94720, USA

³Department of Chemical and Biomolecular Engineering, University of California, Berkeley, California 94720, USA



(Received 30 September 2023; accepted 8 January 2024; published 13 February 2024)

Designing conformationally dynamic molecules that self-assemble into predictable nanostructures remains an important unmet challenge. This paper describes how atomic-scale cryogenic transmission electron microscopy (cryo-TEM) can be used to explore the relationship between molecular structure and self-assembly of block copolymers. We examined sheetlike micelles formed in water using a series of diblock copolypeptoids with the same hydrophilic block and three distinct crystalline hydrophobic blocks. Our cryo-TEM images revealed all the structures share nanoscale features, but differ in their intermolecular packing geometries. Different molecular arrangements, parallel and antiparallel V-shaped crystal motifs, were revealed by two-dimensional atomic-scale through-plane images. However, images from tilted samples revealed an unexpected feature when the hydrophobic polypeptoid block comprised phenyl rings with substituted bromine atoms at the para position. The nanosheets contained atomic-scale corrugations that were absent in the other systems which comprised unsubstituted aliphatic and aromatic side chains. We hypothesize that these corrugations are due to the dipolar characteristics of the brominated phenyl group and interactions between this group and water molecules.

DOI: [10.1103/PhysRevMaterials.8.020301](https://doi.org/10.1103/PhysRevMaterials.8.020301)

I. INTRODUCTION

A fundamental challenge in polymer science is to design molecules that self-assemble to give targeted nanostructures. Synthetic block copolymers comprising chemically distinct blocks that are covalently bonded to each other, self-assemble to give a variety of equilibrium morphologies. The morphologies reflect atomic and molecular scale effects such as chain conformations and intermolecular interactions. They also reflect continuum properties such as interfacial tension and melting enthalpy. Self-assembly can result in one-, two-, or three-dimensional structures (particles, sheets, and fibers), spanning dimensions from nanometers to micrometers. The chains within each microphase may be either crystalline or amorphous.

Amphiphilic block copolymers with crystalline hydrophobic blocks, such as poly(lactic acid) [1–6], metallopolymers like polyferrocenylsilane [7–13], and conjugated polymers like poly(3-hexylthiophene) [14–19], usually form micellar aggregates. The hydrophobic blocks organize into crystalline cores, typically fibers or sheets, stabilized by a corona of

hydrophilic blocks that extend into the aqueous phase; the standard spherical micellar structure is usually incommensurate with crystalline motifs. If the hydrophobic chains are long, then the cores comprise folded chains [20–23]. On the other hand, the hydrophobic chains are short, then they span the micelle cores without folding [24–26].

Polypeptoids are bioinspired short-chain polymers with N-substituted glycine backbones; monomers are distinguished by the chemical structure of the side chains [27,28]. Diblock copolypeptoids with a hydrophilic amorphous block paired with a crystalline hydrophobic block, tend to form planar crystals, notable for their nanometer-scale thickness and micrometer-scale lateral dimensions [24,26,29–39]. The polypeptoid backbones in the crystalline core adopt an all-cis configuration [40,41]. The absence of folded-chain crystals, which can be attributed to relatively short chain lengths, makes them ideal elucidating the principles that govern crystalline self-assembly.

Similar to conventional block copolymers, self-assembly of block copolypeptoids is affected by factors such as chemical structure, molecular topology, and processing conditions. The spatial organization of copolypeptoid molecules in crystalline motifs, dimensions of unit cells, and micelle dimensions have been extensively investigated using approaches such as x-ray and neutron scattering, atomic force microscopy, and transmission electron microscopy (TEM) [32–34,42–51]. Experimental results are often compared with predictions based on molecular dynamic (MD) simulations [26,46,49,52,53]. However, validation of MD simulation results with atomic-scale images of molecular arrangements remains challenging.

*Corresponding author: xijiang@lbl.gov

†Corresponding author: nbalsara@berkeley.edu

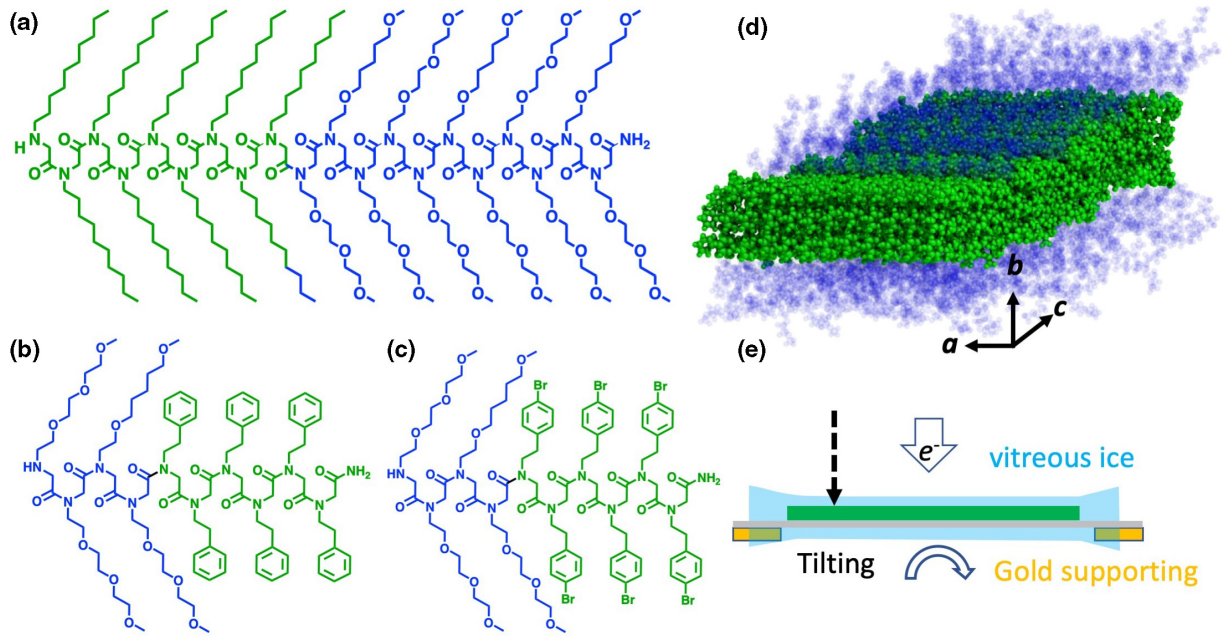


FIG. 1. (a) The chemical structure of the pNte₉-b-pNdc₉ polypeptoid. (b) The chemical structure of the pNte₄-b-pNpe₆ polypeptoid. (c) The chemical structure of the pNte₄-b-pNbrpe₆ polypeptoid. The hydrophilic blocks are shown in blue, and the hydrophobic blocks are shown in green. (d) A schematic of crystallization-driven self-assembled polypeptoid nanosheets in water. (e) A schematic of the cryo-TEM imaging experiments showing the frozen hydrate nanosheets in vitreous ice residing on a custom-built sample support. The sample and continuous carbon film are shown in green and grey, respectively. We discuss micrographs of both untilted and tilted samples.

One challenge in the structural determination of these materials is preserving the original structures that are present in solution. Liquid cell TEM offers insights into the evolution of morphology, but with spatial resolution much lower than the atomic scale [54–58]. Dry samples of self-assembled nanostructures are frequently examined using TEM but the morphology obtained in solutions may undergo changes during the drying process. Additional challenges relate to the electron-beam-induced damage. Since soft materials comprise primarily of light elements, they are vulnerable to ionization radiation damage caused by inelastic electron scattering, which can, in turn, cleave chemical bonds and distort crystalline lattices [59–63]. To avoid this, electron doses below $30 \text{ e}/\text{\AA}^2$ are necessary if the TEM experiments are conducted at liquid nitrogen temperatures (-170°C) [64,65]. The maximum dose reduces by a factor of five if the TEM experiments are conducted at ambient temperatures. A third challenge arises due to the fact that most TEM images, especially those of beam-sensitive soft materials, are two-dimensional (2D) projections. Extrapolating into the third dimension is often based on intuition rather than quantitative data. For example, it is natural to assume that the surfaces of crystalline nanosheet cores are smooth as this would minimize the positive interfacial contribution to the free energy of self-assembly [66]. Electron tomography has provided considerable insight into the nature of soft self-assembled nanostructures in solution, but most studies restricted to length scales that are well above the atomic scale [67–71]. Electron crystallography, an established technique for 3D reconstruction of radiation-sensitive materials like proteins and linear polymers [72–77], hinges on aligning Bragg reflections from electron diffrac-

tion patterns obtained at different tilt angles relative to the incident electron beam. In this paper, we discuss applying this approach to study the atomic-scale structure of crystalline peptoid nanosheets.

Cryo-TEM has emerged as a crucial technique for probing the self-assembled structures formed by radiation-sensitive polymeric materials, for instance, polymer micelles and vesicles [78–88], and addressing the first two challenges described above. Nanostructures in aqueous solutions can be preserved by rapidly “freezing” droplets containing the polymers onto TEM grids using liquid ethane [89,90]. These intact nanostructures, encased in vitreous ice, can be imaged by TEM utilizing direct electron detectors under minimal electron doses (5 to $30 \text{ e}/\text{\AA}^2$). Dose-fractionated movies of images or diffraction patterns are obtained and refined to enhance the signal-to-noise ratio by filtering out the effects of beam-induced motion and mechanical vibrations [91,92]. This approach unveils concealed structural information through 3D reconstruction when paired with specimen tilting.

Our objective is to elucidate the relationship between molecular and crystal structure obtained by self-assembly of three different amphiphilic block copolypeptoids in water. The first polypeptoid comprises an aliphatic hydrophobic block, as depicted in Fig 1(a). It consists of a hydrophobic poly-*N*-decylglycine (pNdc) block with *n*-decyl side chains and a hydrophilic poly-*N*-2-(2-(2-methoxyethoxy)ethoxy)ethylglycine (pNte) block with hydrophilic ethyleneoxy side chains. Both blocks contain nine repeat units, and this polypeptoid is denoted as pNdc₉-b-pNte₉. The chemical structures of the second and third polypeptoids, built upon aromatic hydrophobic

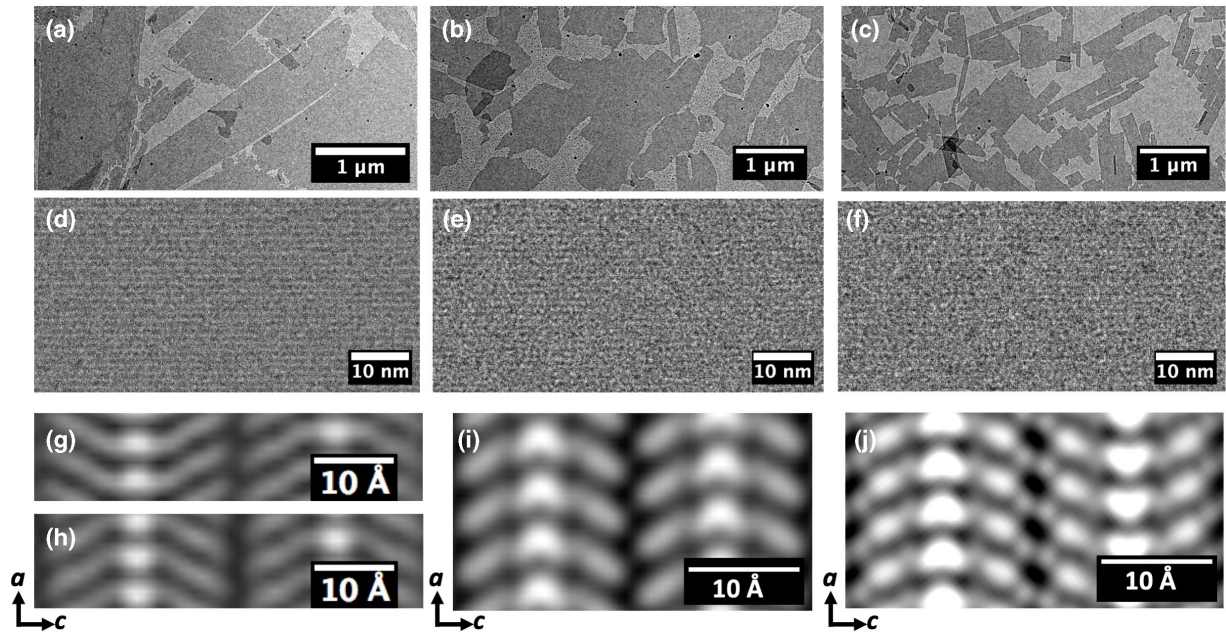


FIG. 2. (a)–(c) show the typical morphology of self-assembled peptoid nanosheets formed by $\text{pNte}_9\text{-b-pNdc}_9$, $\text{pNte}_4\text{-b-pNpe}_6$, $\text{pNte}_4\text{-b-pN4Brpe}_6$, respectively. (d)–(f) Low-dose cryo-TEM micrographs of the nanosheets in (a)–(c), respectively. (g) and (h) Averaged images obtained from $\text{pNdc}_9\text{-b-pNte}_9$ nanosheets showing the antiparallel V-shaped and parallel V-shaped motifs. (i) and (j) Averaged images obtained from the nanosheets formed by $\text{pNte}_4\text{-b-pNpe}_6$, and $\text{pNte}_4\text{-b-pN4Brpe}_6$. In (g)–(j), bright areas represent the electron dense regions. The N-glycine backbones are most electron dense and are located in the middle of the vs. The arms emanated from the vs represent the side-chains. Adapted with permission from Refs. [35,36].

blocks, are illustrated in Figs. 1(b) and 1(c). Both incorporate the same hydrophilic monomers *N*-2-(2-methoxyethoxy)ethoxyethylglycine (pNte) and aromatic hydrophobic monomers *N*-(2-phenylethyl)glycine (pNpe), with a block ratio of four Nte units to six Npe units. Notably, the second polypeptoid possesses hydrogen atoms at the *para* positions of its aromatic rings, whereas the third replaces them with bromine atoms. These two polypeptoid block copolymers are denoted as $\text{pNte}_4\text{-b-pNpe}_6$ and $\text{pNte}_4\text{-b-pN4Brpe}_6$. In all three cases, the crystalline nanosheets are stabilized by hydrophilic pNte blocks [represented by blue chains in Figs. 1(a)–1(d)] that extend into the surrounding water. The hydrophobic crystalline chains, pNdc, pNpe, and pNBrpe, are represented by green chains in Figs. 1(a)–1(d). Figure 1(e) depicts our strategy for achieving atomic-scale images of the crystalline chains, using an ultraflat gold supporting grid that enables high-resolution imaging in both untilted and tilted nanosheets. The objective of this review is to directly compare the data presented in Refs. [35,36,38] to expose the relationship between molecular structure of the hydrophobic peptoid blocks and their arrangement in crystalline nanosheet cores.

II. MOLECULAR STRUCTURE AND THE HETEROGENEITY OF CRYSTAL MOTIFS

The self-assembled nanosheets were created by slow evaporation of polypeptoids from a mixture of water and tetrahydrofuran, yielding an aqueous suspension of peptoid nanosheets. Figures 2(a)–2(c) present electron micrographs of dried nanosheets formed by $\text{pNdc}_9\text{-b-pNte}_9$, $\text{pNte}_4\text{-b-pNpe}_6$ and $\text{pNte}_4\text{-b-pN4Brpe}_6$. The direction of the incident elec-

tron beam is labeled as the *b* direction and the plane of the nanosheets, resting on a carbon support film, are perpendicular to this direction. Figures 2(d)–2(f) display medium-resolution, low-dose cryo-TEM micrographs of vitrified nanosheets formed by $\text{pNdc}_9\text{-b-pNte}_9$, $\text{pNte}_4\text{-b-pNpe}_6$ and $\text{pNte}_4\text{-b-pN4Brpe}_6$. The micrographs from all the samples exhibit characteristic horizontal stripes representing the N-substituted glycine backbones. In all cases, the polypeptoid chains are extended and oriented perpendicular to the plane of the nanosheet. This is anticipated from the geometry of the nanosheet shown in Fig. 1(d).

We use a sorting- and averaging-based approach to determine the crystal motifs. Multiple low-dose cryo-TEM micrographs are obtained from untilted and tilted vitrified nanosheets on ultra-flat gold supports [37]. The unit cell locations in the nanosheets in Figs. 2(d) through F are identified, and the small 2D images (usually $72 \text{ \AA} \times 72 \text{ \AA}$) are extracted from each unit cell's location to obtain boxes containing multiple unit cells [35,93]. Those boxes are classified based on the structure of the crystal. These boxes are then averaged to enhance the signal-to-noise ratio using algorithms described in Ref. [82] to give the crystal structure in the *a-c* plane.

The classification process yielded two distinct classes in unequal abundance in an individual nanosheet formed by $\text{pNdc}_9\text{-b-pNte}_9$: antiparallel V-shaped and parallel V-shaped motifs, where adjacent stacks of molecules are oriented in an opposite manner in the *c* direction. High-resolution micrographs reflect averages of about 100 000 individual images from different nanosheets are shown in Figs. 2(g) and 2(h). In Fig. 2(g), the bright spots signify the end view of the glycine backbones. The V-shaped arms stemming from these spots are

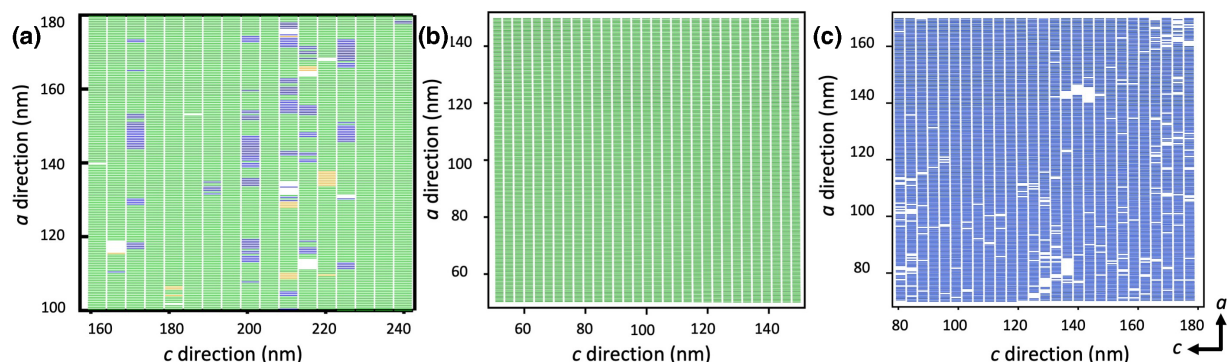


FIG. 3. Distribution maps of crystal motifs and in (a) pNte₉-b-pNdc₉, (b) pNte₄-b-pNpe₆, and (c) pNte₄-b-pN4Brpe₆, respectively. Each individual rectangle in the maps represents an extracted box. Anti-parallel V-shaped motifs in Fig. 2 are shown as blue boxes. Parallel V-shaped motifs are shown as green boxes. Disordered motif is shown as yellow boxes. White areas within the maps represent the regions that could not be analyzed. Adapted with permission from Refs. [35,36].

images of side chains emanating from adjacent monomers. Side chains in neighboring rows adopt an antiparallel alignment. The vertical dark band between adjacent rows of Vs indicates a low electron density gap between neighboring chains. The averaged image of pNdc₉-b-pNte₉ chains in the parallel V-shaped motif is presented in Fig. 2(h), which similar to Fig. 2(g), except for the fact that the adjacent rows of pNdc chains are parallel to each other. Adjacent rows of pNdc chains are shifted relative to one another along the *a* direction, resulting in a unit cell comprising two chains along the *c* direction. Both the parallel and antiparallel V-shaped motifs have the same unit cell size.

In contrast to the heterogeneity in crystalline motifs seen in peptoids with aliphatic side chains, nanosheets formed by peptoids with aromatic side chains display a single motif. The atomic-scale cryo-TEM image of the pNte₄-b-pNpe₆ nanosheet, derived by averaging the unit cells in Fig. 2(e), is shown in Fig. 2(i). The entire crystal in Fig. 2(e) contains unit cells with only the parallel V-shaped molecular arrangement. The unit cell of pNte₄-b-pNpe₆, which also contains two chains in the *c* direction with a dark vertical stripe between them, is smaller than that of the pNdc₉-b-pNte₉ unit cell, primarily because of the differences in side-chain length. The backbones appear bright in Figs. 2(g), 2(h), and 2(i) as expected in the *cis* conformation, but the brightness of the arms of the Vs are a little less uniform in the pNte₄-b-pNpe₆ case. The slight decrease in brightness near the backbone in Fig. 2(i) is attributed to the alkyl link between the backbone and the phenyl group; in Figs. 2(g) and 2(h) the entire side chain is alkyl. The image of the pNte₄-b-pN4Brpe₆ nanosheet is illustrated in Fig. 2(j). Molecules in the pNte₄-b-pN4Brpe₆ unit cell are organized in the antiparallel V-shaped arrangement, as shown in Fig. 2(j). The image of the backbone and aromatic side chains match those in Fig. 2(i). The distinction between the alkyl linkage and the phenyl group is clearly seen in the pNte₄-b-pN4Brpe₆ crystal. In addition, the dark band between the two adjacent chains in the *c* direction is interrupted by spheres that represent the Br atoms.

Figure 3 displays a distribution map indicating the locations of different motifs within an individual nanosheet. In these maps, rectangles symbolize the positions of unit cells. Each rectangle's color represents the local motif

within that box: green for parallel V-shaped motifs, blue for antiparallel V-shaped motifs, and yellow for disordered motifs, while unanalyzed sections, where the lattice structures are less ordered, remain uncolored. Continuous domains of the same-colored boxes represent coherently ordered clusters (grains) of a specific motif. Figure 3(a) reveals that the pNdc₉-b-pNte₉ nanosheet is dominated by parallel V-shaped motifs interspersed with disordered sections and stripes of antiparallel V-shaped motifs. In contrast, Fig. 3(b) illustrates that pNte₄-b-pNpe₆ nanosheets consistently exhibit the parallel V-shaped motif. The pNte₄-b-pN4Brpe₆ nanosheets consistently display the antiparallel V-shaped motif, but with a significant number of unanalyzed sections - see Fig. 3(c).

The uniformity of crystalline motifs appears to be related to the side chain characteristics. Aromatic side chains foster more organized stacking, while two different crystalline motifs were detected in the case of aliphatic side chains. Intriguingly, the crystal motifs in the aromatic nanosheets shift from parallel to antiparallel when the *para* hydrogens on the aromatic rings are replaced by bromine. Covalently bonded Br atoms bonded to C atoms are polarized - a region of positive electrostatic potential develops at the distal end of the otherwise electronegative Br atom (along the direction of the C-Br bond) [94]. By comparing the experimental images with MD simulation results, it was shown that the emergence of an antiparallel crystal motif in pNte₄-b-pN4Brpe₆ nanosheets is due the dipole-dipole interactions [39]. These interactions bring neighboring Br atoms in close proximity, bridging the dark “empty space” between adjacent peptoid chains that is present in non-brominated peptoids (see Fig. 2).

Thus far, conclusions regarding the relationship between molecular structures and their alignment in crystal motifs is based entirely on the 2D projections. This raises a question: Are there any differences between the nanosheets in the third dimension?

III. MOLECULAR STRUCTURE AND THEIR ARRANGEMENTS IN CRYSTAL MOTIFS

The top panels in Figs. 4(a)–4(c) display atomic models of the crystalline hydrophobic peptoid blocks of pNte₄-b-pN4Brpe₆, pNte₄-b-pNpe₆ and pNdc₉-b-pNte₉. We

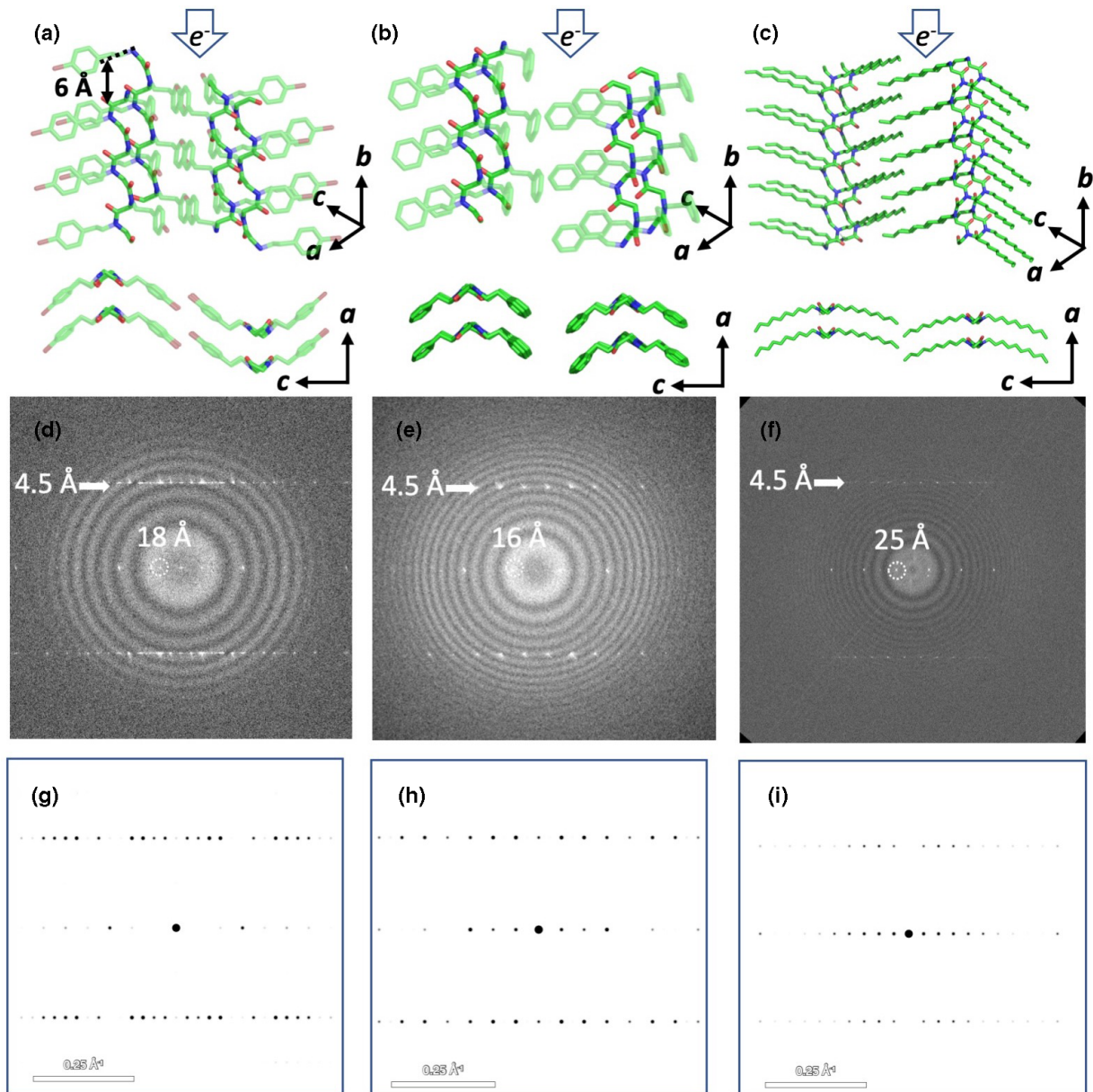


FIG. 4. The relationship between atomic structure of untilted nanosheets and power spectra. (a) The atomic model of the pNte₄-b-pN4Brpe₆ peptoid. 6 Å is the distance between two adjacent phenyl rings on the pN4Brpe₆ side chains. Two adjacent chains in each row are displaced by 6 Å in the *a* direction. (b) and (c) Atomic models of pNte₄-b-pNpe₆ and pNte₉-b-pNdc₉ polypeptoids. Adjacent chains in these peptoids are not displaced in the *a* direction. Only the crystalline peptoid blocks are depicted. Atoms of oxygen, carbon, and nitrogen are colored red, green, and blue, respectively. The top panel illustrates the ordered peptoid molecules that are aligned parallel to the electron beam without tilting, leading to the projections of the *a*-*c* plane. (d) The power spectrum from the low-dose cryo-EM micrograph in Figs. 2(d) displays reflections from the lattice formed by pNte₄-b-pN4Brpe₆ polypeptoids. Thon rings are attributable to the thin carbon support. Reflections at 4.5 Å denote the spacing between two consecutive polypeptoid backbones in a row (*a* direction), as indicated by the arrow. Reflections at 18 Å (as indicated by the dashed circle) represent the spacing between two adjacent rows (*c* direction). (e) The power spectra obtained from the nanosheets formed by pNte₄-b-pNpe₆ polypeptoids. The *a* and *c* spacings are 4.5 Å and 16 Å, respectively. (f) The power spectra obtained from the nanosheets formed by pNte₉-b-pNdc₉ polypeptoids. The *a* spacing remains 4.5 Å while the *c* spacing increases to 25 Å due to the presence of longer side chains. (g) through (i) Simulated electron diffraction patterns based on the models in (a) through (c). The spatial frequencies of reflections agree with the experimental results in (d) to (f). Adapted with permission from Refs. [35,36,38].

show both a 3D view of two adjacent rows of the molecules, as well as the view in the *a*-*c* plane. Power spectra of the low-dose cryo-TEM images obtained from the untilted nanosheets of pNte₄-b-pN4Brpe₆, pNte₄-b-pNpe₆ and pNdc₉-b-pNte₉ are given in Figs. 4(d)–4(f). The series of reflections signifying

the 4.5 Å spacing between two adjacent molecules along the *a* direction is highlighted by an arrow; this reflection is seen in all three samples. In contrast, the *c* spacing, indicating the distance between two molecules along the *c* direction, depends mainly on the length of the side chains, and it is identified by

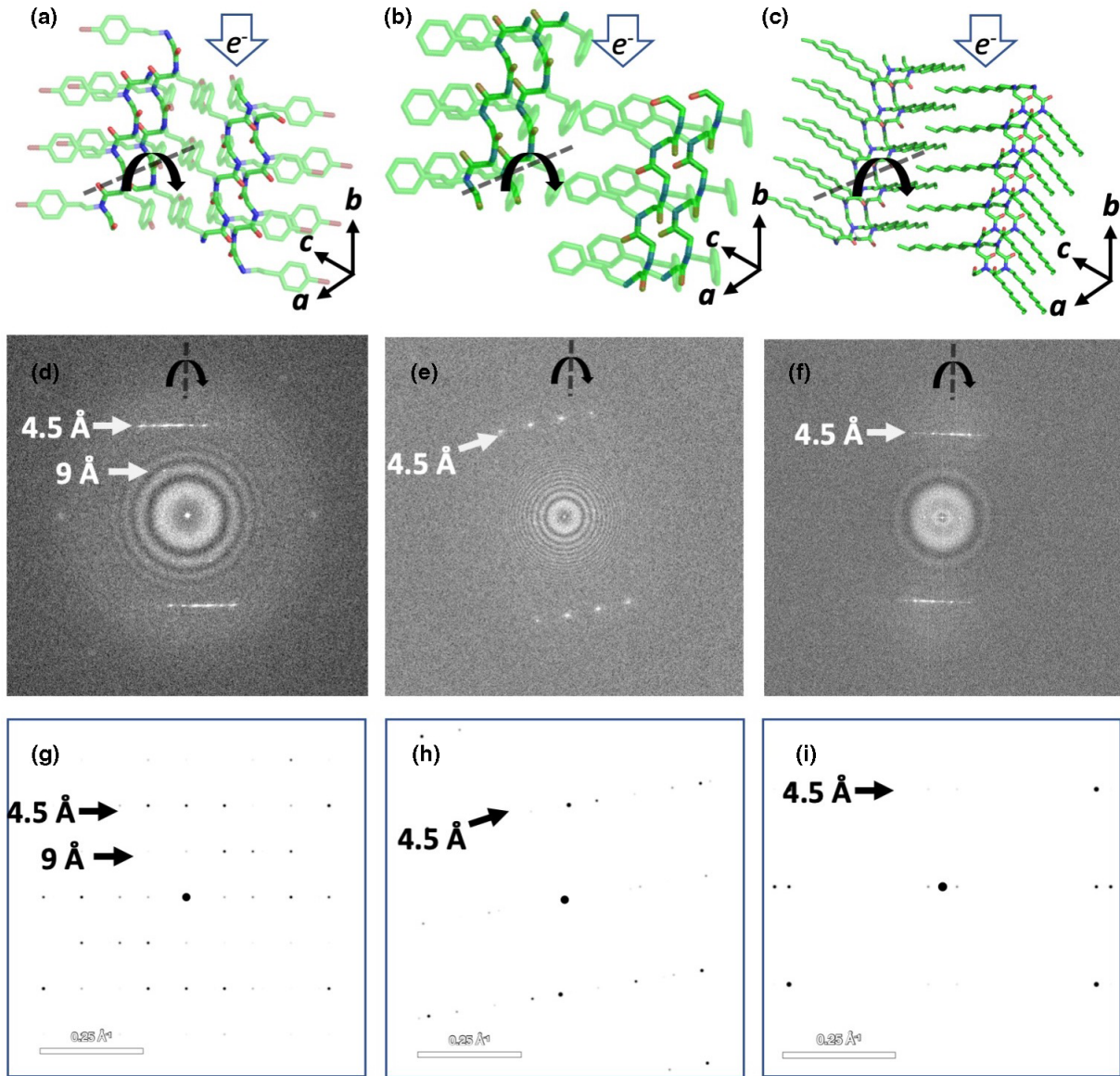


FIG. 5. The relationship between atomic structure of tilted nanosheets and power spectra. The tilt angle is 30° and the tilt axis is shown in the top panels. (a), (b), and (c) Atomic models of tilted crystals of pNte₄-b-pN4Brpe₆, pNte₄-b-pNpe₆ and pNte₉-b-pNdc₉ polypeptoids, respectively. Only the crystalline peptoid blocks are depicted. Atoms of oxygen, carbon, and nitrogen are colored red, green, and blue, respectively. (d) The power spectrum from the low-dose cryo-EM micrograph of a 30° tilted pNte₄-b-pN4Brpe₆ nanosheet. The reflections corresponding to the 4.5 Å row also seen in Fig. 4(d) are detected. In addition, the emergence of new rows of reflections at 9 Å are evident. (e) and (f) The power spectra obtained from the 30° tilted pNte₄-b-pNpe₆ and pNte₉-b-pNdc₉ nanosheet. Only the reflections corresponding to the 4.5 Å row also seen in Figs. 4(e) and 4(f) are detected. (g) Simulated electron diffraction patterns of tilted atomic model of crystal of pNte₄-b-pN4Brpe₆ in (a) showing the rows at 9 Å, consistent with experimental data in (d), (h), and (i). Simulated electron diffraction patterns of tilted atomic models of crystals of pNte₄-b-pNpe₆ and pNte₉-b-pNdc₉ atomic models in (b) and (c). The rows at 9 Å are not visible in both tilted peptoids. Adapted with permission from Refs. [35,36,38].

dashed circles. It is also noteworthy that Figs. 4(e) and 4(f) contain fewer reflections compared to Fig. 4(d), a result of symmetry restrictions stemming from the parallel V-shaped motif relative the antiparallel motif.

To confirm the precision of the atomic models, simulated electron diffraction patterns were calculated, and the results are shown in Figs. 4(g)–4(i). The prominent reflections related to the *a* and *c* spacings, align well with experimental data. Discrepancies in the intensity of reflections exist mainly because the experimental data represent power spectra rather than

electron diffraction patterns. Based on the 2D projections, the determined unit cell dimensions of pN4Brpe₆, pNpe₆, and pNte₉ crystals are $4.5 \times 38 \text{ Å}^2$, $4.5 \times 36 \text{ Å}^2$, and $4.5 \times 50 \text{ Å}^2$.

Figures 5(a)–5(c) show 30° tilted atomic models of the hydrophobic polypeptoid crystals of interest, pN4Brpe₆, pNpe₆, and pNte₉. The tilt axis, indicated by a dashed line, is coincident with the *a* direction. The power spectrum of the low-dose cryo-TEM images from the 30° tilted nanosheets are presented in Figs. 5(d)–5(f). All of the systems exhibit the rows of 4.5 Å reflections identified above. Notably, however,

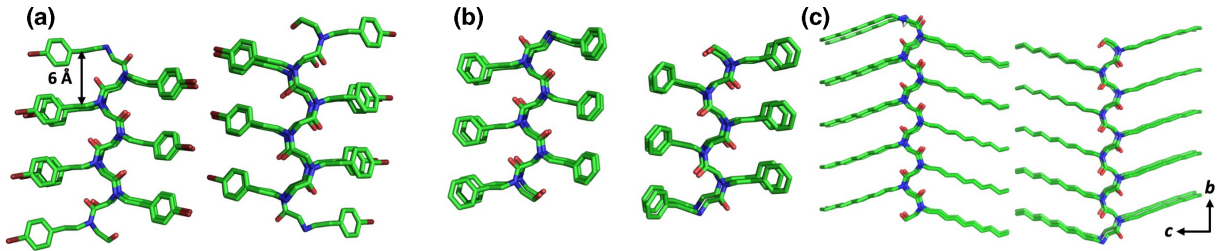


FIG. 6. The b - c plane view of the atomic models of (a) pNdc₉- b -pNte₉, (b) pNte₄- b -N4pe₆, and (c) pNte₄- b -pN4Brpe₆ polypeptoids. Only the crystalline blocks are depicted. Atoms of oxygen, carbon, and nitrogen are colored red, green, and blue, respectively. The 6-Å offset between two molecules along the a direction is indicated in (a).

rows of reflections at 9 Å emerge in the power spectrum of the tilted pN4Brpe₆ nanosheet [Fig. 5(d)]. This characteristic is not observed in the untilted crystal of pN4Brpe₆ [Fig. 4(d)] nor is it present in any of the images of other peptoids, tilted or untilted.

Since the 30° tilted pNte₄- b -pN4Brpe₆ nanosheets exhibited obvious new features, we obtained averaged images from hundreds different nanosheets with at different tilt angles [38]. These images were evaluated using a hybrid electron crystallographic technique which includes single-particle analysis

to increase the spatial resolution [95]. The spacing between each monomer along the chain axis is 6 Å (the bond lengths involved are well established) and adjacent chains along the a direction are displaced relative to each other by two monomer [40]. This displacement is shown in the atomic model in Fig. 4(a). The displacement is also shown in Fig. 5(a) but is more difficult to discern due to the tilted nature of the crystal. The correct unit cell dimensions in the a - c plane in pN4Brpe₆ crystals is thus 9 Å × 36 Å. The simulated diffraction patterns from the pNte₄- b -pN4Brpe₆ model presented in Fig. 5(g) confirms this conclusion.

There are no unique features observed in the tilted nanosheets of pNte₄- b -pNpe₆ and pNdc₉- b -pNte₉. We conclude on this basis that the nanosheets in these samples are smooth and uncorrugated. The main difference in the crystal structure of pN4Brpe₆, pNpe₆, and pNte₉ is in the b direction, which is hidden in the through-plane projections. The bromine atoms at the para position of phenyl side chains not only influence the packing in the c direction (parallel vs unparallel V-shaped motif) but also the b direction (offset vs no offset).

For clarity, the atomic models of the crystals viewed in the b - c plane (through plane images) are shown in Fig. 6. The pNte chains solubilizing the nanosheets emanate from opposite ends of the crystal (not shown since they are amorphous and thus not visible). We show two sets of chains, one in the front and one in the back. In the case of pNpe₆ and pNte₉, the two chains are aligned. In the case of pN4Brpe₆ [Fig. 6(a)], there is an offset of 6 Å, such that there is less molecular overlap between two adjacent chains. It is evident that replacing the bromine atoms in the *para* position of the phenyl rings results in a significant difference in the nanoscale morphology of the nanosheets.

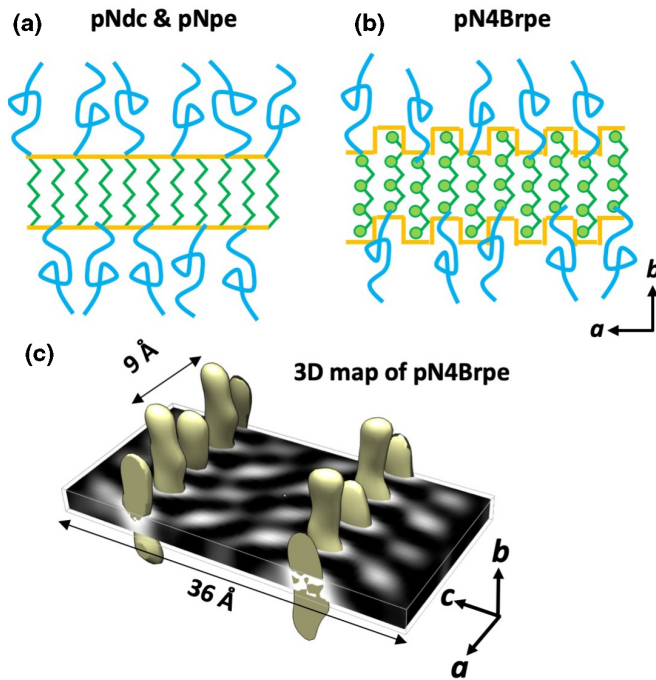
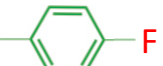

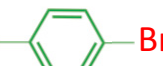

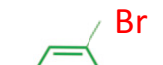





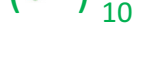


FIG. 7. Schematics of side views of the crystalline cores of sheet-like micelles in water. The block copolymers studied were (a) pNdc₉- b -pNte₉, pNte₄- b -N4pe₆, and (b) pNte₄- b -pN4Brpe₆. Only the crystalline blocks are shown. The bromine atoms are shown as spheres while the other parts of the hydrophobic chains are represented by zig-zag lines. The blue curves represent the pNte blocks extending into the aqueous phase. The straight and corrugated interfaces are shown in yellow. The pN4Brpe nanosheets exhibit periodic atomic-scale corrugations while the other nanosheets are smooth. (c) Visualized backbones of the pN4Brpe₆ blocks overlay on the tomographic slice in the a - c plane in Ref. [38].

IV. SUMMARY AND PERSPECTIVE

The purpose of this paper is to illustrate the use of atomic scale cryo-TEM for studying the effect of molecular structure on block copolymer self-assembly. We studied the formation of sheetlike micelles in water using a series of diblock copolypeptoids with Nte hydrophilic blocks and three different crystalline hydrophobic blocks. Most TEM images of polymers in the literature are obtained by microtoming into thin sections. The sheetlike structure of the micelles in the series of polypeptoids make them ideally suited for atomic-scale TEM; thin sections are obtained by self-assembly. However, it is not trivial to probe the structure of the micelle in the

TABLE I. The summary of XRD peaks around 9 Å observed in literature.

End Group of the side chain	Observation of XRD peak at about 9 Å
	No, weak peak at 8.2 Å, ref. [36].
	Yes, weak peak at 9 Å, ref. [36].
	Yes, weak peak 9 Å, ref. [32].
	Yes, weak peak at 9 Å, ref. [49].
	Yes, strong peak at 9.2 Å, ref. [38].
	Yes, strong peak at 9.1 Å, ref. [46].
	Yes, strong peak at 9.2 Å, ref. [49].
	Yes, strong peak at 9.5 Å, ref. [36].
	Yes, strong peak at 9.5 Å, ref. [49].
	Yes, weak peak at 9 Å, ref. [36].
	Yes, very weak peak at 9 Å, ref. [36].
	No, weak peak at 8.1 Å is observed, ref. [36] and ref. [98].
	No, weak peak at 6.5 Å, ref. [43].
	No, weak peak at 8.0 Å, ref. [43].
	No, weak peak at 10 Å, ref. [43].
	No, weak peak at 12.3 Å, ref. [40].
	strong peak at 12 Å, ref. [43].

direction perpendicular to the sheet; this paper focuses on information that may be buried along this direction. We obtained this information by tilting the sheet, a standard operation in electron crystallography studies of planar polymer crystals [72,73,90,96]. However, obtaining atomic-scale data required building a custom sample support that prevented crinkling of the sample when it is cooled to cryogenic temperatures [37,97].

Many features of the nanosheets formed by pNte₄-b-pN4Brpe₆, pNte₄-b-pNpe₆ and pNdc₉-b-pNte₉ were evident in the through-plane images of the *a*-*c* plane. The primary motif of pNpe₆ and pNte₉ crystals was the parallel V-shaped motif while that in the pN4Brpe₆ antiparallel V-shaped motif. There are also differences in the defect densities and types in the nanosheets, but whether these differences are related to differences in chemical structure or small unavoidable differences in processing remains unclear.

The most important difference between the systems was, however, hidden in the *b* direction.

Atomic-scale corrugations were detected in pNte₄-b-pN4Brpe₆ nanosheets but not in pNte₄-b-pNpe₆ and pNdc₉-b-pNte₉. This qualitative difference is depicted schematically in Fig. 7. In Fig. 7 A, we show simple a sheetlike micelle that is representative of micelles formed by pNte₄-b-pNpe₆ and pNdc₉-b-pNte₉. The fact that crystals of soft polymers would not be perfectly flat is to be expected due to thermal fluctuations, motion of the chains that form the crystal, and finite concentration of defects. However, the presence of periodic corrugations as shown in Fig. 7 B which is representative of a sheetlike micelle formed by pNte₄-b-pN4Brpe₆ is entirely unexpected. The 3D structure of these micelles is clarified in Fig. 7(c). The noteworthy feature in these micelles is the presence of a 9 Å feature which is absent in the noncorrugated sheets.

The extent to which corrugated sheetlike micelles are obtained from other systems remains to be established. The standard approach for determining crystal structure is x-ray diffraction (XRD); we are not aware of any other cryo-EM studies of polypeptoid crystals. Since the *a* spacing in virtually all peptoid crystals is 4.5 Å [40], we examined the polypeptoid literature for the presence of a diffraction peak in the vicinity of *d* = 9 Å (i.e., a peak located at *q* = 0.7 Å⁻¹, where *q* is the magnitude of the scattering vector). The results of this literature survey are summarized in Table I where we give the chemical structure of the terminus of polypeptoid side chain and the relevant XRD data. When diffraction peaks in the vicinity of *d* = 9 Å were reported, we categorized the peaks as weak or strong based on its intensity (some personal judgment was exercised). Peaks outside the 9.0 ± 0.5 Å range were ignored; in all cases when these peaks were detected they were either weak or very weak. It is evident from the data in Table I that the *d* = 9 Å peak is only obtained in peptoids with halogenated phenyl groups at the termini of the side chains. Different explanations for the existence of this feature were proposed by the authors. In a number of cases [32,36,38,46], the peak was interpreted as the second-order Bragg reflection corresponding to the distance between adjacent backbones in the *c* direction. In the case of pNte₄-b-pN4Brpe₆, the *d* = 9 Å peak is exactly where this second-order reflection is expected (the distance between adjacent backbones in the *c*-direction is 18 Å). In Ref. [49], the *d* = 9 Å peak was attributed to the herringbonelike structure of the side chains. Definitive determination of crystal structure based on XRD alone is difficult, especially in the case of beam-sensitive soft materials. 3D cryo-EM at the atomic scale may be necessary to determine the origins of the observed diffraction peak at 9 Å in different peptoid systems.

One of the factors that dictates the equilibrium morphology of micellar structures is interfacial tension between the core and the solvated corona. This contribution will be minimized by interfaces that are, on average, smooth. It is commonly assumed that the core-corona interfaces in all micelles—spherical, cylindrical or sheet-like micelles—are smooth on average [66]. The interfacial area in the corrugated micelle shown in Figs. 7(b) and 7(c) is a factor of 2 larger than that in the smooth micelle. To our knowledge, the prevailing theories of micelle formation have not anticipated such

a result. We hypothesize that the corrugations are the result of the dipolar nature of the brominated phenyl group in pNte₄-b-pN4Brpe₆. The interactions between this dipolar group and water molecules appear to be more favorable when compared with those between more commonly used nonpolar aliphatic and aromatic groups. Incorporating these kinds of specific interactions in theories of micelle self-assembly seems warranted. In the long run, we hope that images of soft matter at the atomic scale will enable an improved understanding of nonbonded interactions in these systems.

ACKNOWLEDGMENTS

Primary funding for this work was provided by the Soft Matter Electron Microscopy Program (KC11BN), supported by the Office of Science, Office of Basic Energy Science, U.S. Department of Energy, under Contract No. DE-AC02-05CH11231. Work at the Molecular Foundry was supported by the Office of Science, Office of Basic Energy Sciences, of the U.S. Department of Energy under Contract No. DE-AC02-05CH11231.

The authors declare no competing financial interest.

- [1] N. Petzetakis, D. Walker, A. P. Dove, and R. K. O'Reilly, *Soft Matter* **8**, 7408 (2012).
- [2] T. Fujiwara, M. Miyamoto, Y. Kimura, T. Iwata, and Y. Doi, *Macromolecules* **34**, 4043 (2001).
- [3] X. M. He, M. S. Hsiao, C. E. Boott, R. L. Harniman, A. Nazemi, X. Y. Li, M. A. Winnik, and I. Manners, *Nat. Mater.* **16**, 481 (2017).
- [4] D. Portinha, F. Boue, L. Bouteiller, G. Carrot, C. Chassenieux, S. Pensec, and G. Reiter, *Macromolecules* **40**, 4037 (2007).
- [5] L. Sun, N. Petzetakis, A. Pitto-Barry, T. L. Schiller, N. Kirby, D. J. Keddie, B. J. Boyd, R. K. O'Reilly, and A. P. Dove, *Macromolecules* **46**, 9074 (2013).
- [6] P. J. Hurst, A. M. Rakowski, and J. P. Patterson, *Nat. Commun.* **11**, 4690 (2020).
- [7] L. Cao, I. Manners, and M. A. Winnik, *Macromolecules* **35**, 8258 (2002).
- [8] Z. M. Hudson, C. E. Boott, M. E. Robinson, P. A. Rupar, M. A. Winnik, and I. Manners, *Nat. Chem.* **6**, 893 (2014).
- [9] J. J. Jiang, E. Nikbin, G. Hicks, S. F. Song, Y. Liu, E. C. N. Wong, I. Manners, J. Y. Howe, and M. A. Winnik, *J. Am. Chem. Soc.* **145**, 1247 (2023).
- [10] S. Pearce, X. M. He, M. S. Hsiao, R. L. Harniman, L. R. MacFarlane, and I. Manners, *Macromolecules* **52**, 6068 (2019).
- [11] H. B. Qiu, Y. Gao, C. E. Boott, O. E. C. Gould, R. L. Harniman, M. J. Miles, S. E. D. Webb, M. A. Winnik, and I. Manners, *Science* **352**, 697 (2016).
- [12] H. Wang, M. A. Winnik, and I. Manners, *Macromolecules* **40**, 3784 (2007).
- [13] X. S. Wang, G. Guerin, H. Wang, Y. S. Wang, I. Manners, and M. A. Winnik, *Science* **317**, 644 (2007).
- [14] V. Ho, B. W. Boudouris, B. L. McCulloch, C. G. Shuttle, M. Burkhardt, M. L. Chabiny, and R. A. Segalman, *J. Am. Chem. Soc.* **133**, 9270 (2011).
- [15] D. H. Kim, J. T. Han, Y. D. Park, Y. Jang, J. H. Cho, M. Hwang, and K. Cho, *Adv. Mater.* **18**, 719 (2006).
- [16] J. S. Liu, E. Sheina, T. Kowalewski, and R. D. McCullough, *Angew. Chem. Int. Ed.* **41**, 329 (2002).
- [17] S. Yang and T. L. Choi, *Chem. Sci.* **11**, 8416 (2020).
- [18] S. Yang, S. Y. Kang, and T. L. Choi, *J. Am. Chem. Soc.* **141**, 19138 (2019).
- [19] S. Yang, S. Y. Kang, and T. L. Choi, *Nat. Commun.* **12**, 2602 (2021).
- [20] J. R. Finnegan, X. M. He, S. T. G. Street, J. D. Garcia-Hernandez, D. W. Hayward, R. L. Harniman, R. M. Richardson, G. R. Whittell, and I. Manners, *J. Am. Chem. Soc.* **140**, 17127 (2018).
- [21] E. Mena-Osteritz, A. Meyer, B. M. W. Langeveld-Voss, R. A. J. Janssen, E. W. Meijer, and P. Bäuerle, *Angew. Chem. Int. Ed.* **39**, 2679 (2000).
- [22] T. Vilgis and A. Halperin, *Macromolecules* **24**, 2090 (1991).
- [23] J. Tian, S. H. Xie, U. Borucu, S. X. Lei, Y. F. Zhang, and I. Manners, *Nat. Mater.* **22**, 786 (2023).
- [24] K. T. Nam *et al.*, *Nat. Mater.* **9**, 454 (2010).
- [25] R. Kudirka, H. Tran, B. Sanii, K. T. Nam, P. H. Choi, N. Venkateswaran, R. Chen, S. Whitelam, and R. N. Zuckermann, *Biopolymers* **96**, 586 (2011).
- [26] R. V. Mannige, T. K. Haxton, C. Proulx, E. J. Robertson, A. Battigelli, G. L. Butterfoss, R. N. Zuckermann, and S. Whitelam, *Nature (London)* **526**, 415 (2015).
- [27] K. Kirshenbaum, A. E. Barron, R. A. Goldsmith, P. Armand, E. K. Bradley, K. T. V. Truong, K. A. Dill, F. E. Cohen, and R. N. Zuckermann, *Proc. Nat. Acad. Sci. USA* **95**, 4303 (1998).
- [28] J. Sun and R. N. Zuckermann, *ACS Nano* **7**, 4715 (2013).
- [29] B. Sanii *et al.*, *J. Am. Chem. Soc.* **133**, 20808 (2011).
- [30] E. J. Robertson, G. K. Oliver, M. Qian, C. Proulx, R. N. Zuckermann, and G. L. Richmond, *Proc. Nat. Acad. Sci. USA* **111**, 13284 (2014).
- [31] J. Sun, A. A. Teran, X. X. Liao, N. P. Balsara, and R. N. Zuckermann, *J. Am. Chem. Soc.* **136**, 2070 (2014).
- [32] H. Jin, F. Jiao, M. D. Daily, Y. Chen, F. Yan, Y.-H. Ding, X. Zhang, E. J. Robertson, M. D. Baer, and C.-L. Chen, *Nat. Commun.* **7**, 12252 (2016).
- [33] H. Jin, Y.-H. Ding, M. Wang, Y. Song, Z. Liao, C. J. Newcomb, X. Wu, X.-Q. Tang, Z. Li, Y. Lin, F. Yan, T. Jian, P. Mu, and C.-L. Chen, *Nat. Commun.* **9**, 270 (2018).
- [34] N. S. Jiang, T. Y. Yu, O. A. Darvish, S. Qian, I. K. M. Tsengam, V. John, and D. H. Zhang, *Macromolecules* **52**, 8867 (2019).
- [35] X. Jiang, S. Xuan, J. Kundu, D. Prendergast, R. N. Zuckermann, and N. P. Balsara, *Soft Matter* **15**, 4723 (2019).
- [36] S. T. Xuan, X. Jiang, R. K. Spencer, N. K. Li, D. Prendergast, N. P. Balsara, and R. N. Zuckermann, *Proc. Nat. Acad. Sci. USA* **116**, 22491 (2019).
- [37] X. Jiang, S. T. Xuan, R. N. Zuckermann, R. M. Glaeser, K. H. Downing, and N. P. Balsara, *Microsc. Microanal.* **27**, 767 (2021).
- [38] X. Jiang, M. Seidler, G. L. Butterfoss, X. B. Luo, T. Y. Yu, S. T. Xuan, D. Prendergast, R. N. Zuckermann, and N. P. Balsara, *Acs Macro Letters* **12**, 632 (2023).
- [39] M. Seidler, N. K. Li, X. B. Luo, S. T. Xuan, R. N. Zuckermann, N. P. Balsara, D. Prendergast, and X. Jiang, *J. Phys. Chem. B* **126**, 4152 (2022).

- [40] D. R. Greer, M. A. Stolberg, J. Kundu, R. K. Spencer, T. Pascal, D. Prendergast, N. P. Balsara, and R. N. Zuckermann, *J. Am. Chem. Soc.* **140**, 827 (2018).
- [41] D. R. Greer, M. A. Stolberg, S. Xuan, X. Jiang, N. P. Balsara, and R. N. Zuckermann, *Macromolecules* **51**, 9519 (2018).
- [42] C. U. Lee, T. P. Smart, L. Guo, T. H. Epps, and D. H. Zhang, *Macromolecules* **44**, 9574 (2011).
- [43] C. U. Lee, L. Lu, J. H. Chen, J. C. Garno, and D. H. Zhang, *ACS Macro Letters* **2**, 436 (2013).
- [44] F. Jiao, X. P. Wu, T. Y. Jian, S. Zhang, H. B. Jin, P. G. He, C. L. Chen, and J. J. De Yoreo, *Angew. Chem. Int. Ed.* **58**, 12223 (2019).
- [45] Y. H. Wei, J. L. Tian, Z. K. Zhang, C. H. Zhu, J. Sun, and Z. B. Li, *Macromolecules* **52**, 1546 (2019).
- [46] M. Zhao, S. Zhang, R. Zheng, S. Alamdari, C. J. Mundy, J. Pfandtner, L. D. Pozzo, C.-L. Chen, J. J. De Yoreo, and A. L. Ferguson, *Biomacromolecules* **24**, 2618 (2021).
- [47] N. A. Merrill, F. Yan, H. B. Jin, P. Mu, C. L. Chen, and M. R. Knecht, *Nanoscale* **10**, 12445 (2018).
- [48] H. B. Jin, T. Y. Jian, Y. H. Ding, Y. L. Chen, P. Mu, L. Wang, and C. L. Chen, *Biopolymers* **110**, e23258 (2019).
- [49] J. A. Hammons, M. D. Baer, T. Y. Jian, J. R. I. Lee, T. M. Weiss, J. J. De Yoreo, A. Noy, C. L. Chen, and A. Van Buuren, *J. Phys. Chem. Lett.* **12**, 6126 (2021).
- [50] X. Jiang, R. K. Spencer, J. Sun, C. Ophus, R. N. Zuckermann, K. H. Downing, and N. P. Balsara, *J. Phys. Chem. B* **123**, 1195 (2019).
- [51] J. Sun, Z. W. Wang, C. H. Zhu, M. Y. Wang, Z. K. Shi, Y. H. Wei, X. H. Fu, X. S. Chen, and R. N. Zuckermann, *Proc. Nat. Acad. Sci. USA* **117**, 31639 (2020).
- [52] B. C. Hudson, A. Battigelli, M. D. Connolly, J. Edison, R. K. Spencer, S. Whitelam, R. N. Zuckermann, and A. K. Paravastu, *J. Phys. Chem. Lett.* **9**, 2574 (2018).
- [53] T. Y. Yu, X. B. Luo, D. Prendergast, G. L. Butterfoss, B. Rad, N. P. Balsara, R. N. Zuckermann, and X. Jiang, *Acs Nano* **17**, 4958 (2023).
- [54] J. Park, H. Park, P. Ercius, A. F. Pegoraro, C. Xu, J. W. Kim, S. H. Han, and D. A. Weitz, *Nano Lett.* **15**, 4737 (2015).
- [55] S. D. Pu, C. Gong, and A. W. Robertson, *R. Soc. Open Sci.* **7**, 191204 (2020).
- [56] J. Park, K. Koo, N. Noh, J. H. Chang, J. Y. Cheong, K. S. Dae, J. S. Park, S. Ji, I.-D. Kim, and J. M. Yuk, *ACS Nano* **15**, 288 (2021).
- [57] H. L. Wu, H. Friedrich, J. P. Patterson, N. A. J. M. Sommerdijk, and N. de Jonge, *Adv. Mater.* **32**, 2001582 (2020).
- [58] A. Rizvi, J. T. Mulvey, B. P. Carpenter, R. Talosig, and J. P. Patterson, *Chem. Rev.* **121**, 14232 (2021).
- [59] D. T. Grubb, *J. Mater. Sci.* **9**, 1715 (1974).
- [60] J. R. Fryer, *Ultramicroscopy* **14**, 227 (1984).
- [61] R. F. Egerton, P. Li, and M. Malac, *Micron* **35**, 399 (2004).
- [62] R. F. Egerton, *Ultramicroscopy* **127**, 100 (2013).
- [63] Z. J. W. A. Leijten, A. D. A. Keizer, G. de With, and H. Friedrich, *J. Phys. Chem. C* **121**, 10552 (2017).
- [64] R. Henderson and R. M. Glaeser, *Ultramicroscopy* **16**, 139 (1985).
- [65] R. M. Glaeser, G. McMullan, A. R. Faruqi, and R. Henderson, *Ultramicroscopy* **111**, 90 (2011).
- [66] J. N. Israelachvili, *Intermolecular and Surface Forces* (Academic Press, Burlington, MA, 2011), 3rd ed.
- [67] H. Friedrich, P. M. Frederik, G. de With, and N. A. J. M. Sommerdijk, *Angew. Chem. Int. Ed.* **49**, 7850 (2010).
- [68] M. J. M. Wirix, P. H. H. Bomans, H. Friedrich, N. A. J. M. Sommerdijk, and G. de With, *Nano Lett.* **14**, 2033 (2014).
- [69] J. E. Evans and H. Friedrich, *MRS Bull.* **41**, 516 (2016).
- [70] B. E. McKenzie, J. F. de Visser, G. Portale, D. Hermida-Merino, H. Friedrich, P. H. H. Bomans, W. Bras, O. R. Monaghan, S. J. Holder, and N. A. J. M. Sommerdijk, *Soft Matter* **12**, 4113 (2016).
- [71] R. P. M. Lafleur, S. Herziger, S. M. C. Schoenmakers, A. D. A. Keizer, J. Jahzerah, B. N. S. Thota, L. Su, P. H. H. Bomans, N. A. J. M. Sommerdijk, A. R. A. Palmans, R. Haag, H. Friedrich, C. Böttcher, and E. W. Meijer, *J. Am. Chem. Soc.* **142**, 17644 (2020).
- [72] B. Moss, D. L. Dorset, J. C. Wittmann, and B. Lotz, *J. Polym. Sci. B* **22**, 1919 (1984).
- [73] D. L. Dorset, *Proc. Nat. Acad. Sci. USA* **88**, 5499 (1991).
- [74] D. L. Dorset, W. F. Tivol, and J. N. Turner, *Ultramicroscopy* **38**, 41 (1991).
- [75] D. L. Dorset, *Micron* **25**, 423 (1994).
- [76] T. Walz and N. Grigorieff, *J. Struct. Biol.* **121**, 142 (1998).
- [77] J. M. Baldwin, R. Henderson, E. Beckman, and F. Zemlin, *J. Mol. Biol.* **202**, 585 (1988).
- [78] S. Jain and F. S. Bates, *Science* **300**, 460 (2003).
- [79] C. Liu, M. A. Hillmyer, and T. P. Lodge, *Langmuir* **24**, 12001 (2008).
- [80] N. Saito, C. Liu, T. P. Lodge, and M. A. Hillmyer, *ACS Nano* **4**, 1907 (2010).
- [81] Y. Y. Won, A. K. Brannan, H. T. Davis, and F. S. Bates, *J. Phys. Chem. B* **106**, 3354 (2002).
- [82] Y. Y. Won, H. T. Davis, and F. S. Bates, *Science* **283**, 960 (1999).
- [83] Y. Zheng, Y. Y. Won, F. S. Bates, H. T. Davis, L. E. Scriven, and Y. Talmon, *J. Phys. Chem. B* **103**, 10331 (1999).
- [84] Y. Talmon, H. T. Davis, L. E. Scriven, and E. L. Thomas, *Rev. Sci. Instrum.* **50**, 698 (1979).
- [85] Y. Talmon, D. F. Evans, and B. W. Ninham, *Science* **221**, 1047 (1983).
- [86] E. Kesselman, Y. Talmon, J. Bang, S. Abbas, Z. B. Li, and T. P. Lodge, *Macromolecules* **38**, 6779 (2005).
- [87] H. Cui, T. K. Hodgdon, E. W. Kaler, L. Abezgauz, D. Danino, M. Lubovsky, Y. Talmon, and D. J. Pochan, *Soft Matter* **3**, 945 (2007).
- [88] H. G. Cui, Z. Y. Chen, S. Zhong, K. L. Wooley, and D. J. Pochan, *Science* **317**, 647 (2007).
- [89] K. A. Taylor and R. M. Glaeser, *J. Ultrastruct. Res.* **55**, 448 (1976).
- [90] R. M. Glaeser, *Electron Crystallography of Biological Macromolecules* (Oxford University Press, Oxford, 2007).
- [91] S. Q. Zheng, E. Palovcak, J. P. Armache, K. A. Verba, Y. F. Cheng, and D. A. Agard, *Nat. Methods* **14**, 331 (2017).
- [92] W. J. Zhou, B. Bammes, P. G. Mitchell, K. Betz, and W. Chiu, *Ultramicroscopy* **232**, 113417 (2022).
- [93] X. Jiang, D. R. Greer, J. Kundu, C. Ophus, A. M. Minor, D. Prendergast, R. N. Zuckermann, N. P. Balsara, and K. H. Downing, *Macromolecules* **51**, 7794 (2018).
- [94] G. Cavallo, P. Metrangolo, R. Milani, T. Pilati, A. Priimagi, G. Resnati, and G. Terraneo, *Chem. Rev.* **116**, 2478 (2016).
- [95] R. D. Righetto, N. Biyani, J. Kowal, M. Chami, and H. Stahlberg, *Nat. Commun.* **10**, 1722 (2019).

- [96] W. Y. Chen, C. Y. Li, J. X. Zheng, P. Huang, L. Zhu, Q. Ge, R. P. Quirk, B. Lotz, L. Deng, Chi Wu, E. L. Thomas, and S. Z. D. Cheng, [Macromolecules](#) **37**, 5292 (2004).
- [97] F. P. Booy and J. B. Pawley, [Ultramicroscopy](#) **48**, 273 (1993).
- [98] A. M. Rosales, H. K. Murnen, R. N. Zuckermann, and R. A. Segalman, [Macromolecules](#) **43**, 5627 (2010).